Astronomy & Astrophysics manuscript no. PICOFLARES_2nd_REVISION_BOLD_ALL_CHANAGES_FULL_DRAFT_1stAtt

December 2, 2025

Picoflares in the Quiet Solar Corona

Solar Orbiter Observations from 0.556 AU at the Deep Solar Minimum

O. Podladchikova[1,2,3,⋆], A. Warmuth[2], L. Harra[3,4], L. Dolla[5], C. Verbeeck[5], M. Mierla[5,6], L. Rodriguez[5], S. Parenti[7], M. K. Georgoulis[8,9], S. J. Hofmeister[10,2], N. Engler[3,4], M. J. West[11], A. M. Veronig[12,13], P. Antolin[14], S. Purkhart[12], D. M. Long[15], É. Buchlin[7], M. Haberreiter[3], A. N. Zhukov[5,16], H. Safari[17], A. F. Battaglia[4,18], E. Soubrié[7,19], V. Büchel[3,20], S. Gissot[5], A. De Groof[22], M. Gyo[3], J. P. Halain[11,23], B. Inhester[21], E. Kraaikamp[5], D. Müller[11], D. Pfiffner[20], P. Rochus[23], F. Schuller[2], P. J. Smith[15], W. Schmutz[3,4], and K. Stegen[5]

(Affiliations can be found after the references)

Received ...; accepted...

ABSTRACT

ontext. X-ray observations of the Sun prompted Eugene Parker to introduce the concept of "nanoflares" as fundamental energy release units n the solar corona, with estimated energies of 10^{24} erg from current dissipation in 10,000 km loops. Parker anticipated that even smaller flares ould be detectable with improved instrumentation. A decade later, EUV solar imagers onboard SOHO confirmed this prediction, establishing the etection threshold for the smallest solar flares observed from 1 AU.

ims. On May 30, 2020, the Solar Orbiter's High-Resolution Imager (HRI_{EUV}) operating halfway to the Sun (0.556 AU) during deep solar minimum detected numerous quiet sun small-scale heating events termed "campfires," exhibiting smaller spatial and temporal scales than traditional anoflares. This work extends the statistical analysis of Paper I (Berghmans et al. (2021)) by performing comprehensive thermal energy calculations using the established geometrical and thermodynamic parameters from Paper I while implementing multiple volume models to address the rimary challenge of energy estimation in optically thin coronal plasma.

ethods. We analyze the May 30, 2020 HRI_{EUV} complete event family, including 1,467 HRI_{EUV}-detected campfires ($\geq 5\sigma$ threshold) with stablished parameters and extend to 12,107 events ($\geq 3\sigma$ threshold) to capture weaker events. Three distinct geometrical models (elliptical loop nd two cube models) are implemented to quantify volume uncertainties. Our analysis demonstrates that while absolute energy values show model ependence, the power-law character of energy distributions remains robust across all volume assumptions.

esults. Thermal energies span the picoflare range from 3×10^{20} to 1×10^{24} erg. Occurrence rates are 3×10^{-21} s^{-1} cm^{-2} for $\geq 5\sigma$ events and $\times 10^{-20}$ s^{-1} cm^{-2} for $\geq 3\sigma$ events. Frequency distributions follow power laws with indices $\alpha = 2.32$ ($\geq 5\sigma$) and $\alpha = 2.74$ ($\geq 3\sigma$). The flare nature f these events is confirmed through both thermodynamic parameter trends (EM-T relation following established flare scaling) and characteristic ower-law energy distributions. Event durations (1-260 s) reveal two distinct populations: rapid reconnection events (1-10 s, Alfvénic timescales) nd slower parallel current dissipation (10-100 s, sound-speed timescales).

onclusions. Picoflares extend the solar flare energy continuum to lower energies and higher frequencies, contributing cumulatively 1% of the otal quiet Sun coronal heating power. The detected picoflare rate represents approximately 60 times higher occurrence than previous EUV studies bserved from 1 AU and five orders of magnitude increase over early hard X-ray observations, establishing picoflares as significant energy budget omponents that require additional physical mechanisms beyond traditional nanoflare models for complete coronal heating explanation.

ey words. Sun: corona – Sun: UV radiation – techniques: image processing – plasmas – Sun: flares – Sun: coronal heating – instrumentation: UV

. Introduction

olar flares are observed across a broad spectrum of energies, rom 10^{24} to 10^{33} ergs, over time scales ranging from minutes to ours. Smaller-scale events occur more frequently. Flares with nergies of 10^{27} ergs were first detected in hard X-rays (Lin et al. 1984), while smaller soft X-ray flares were discovered in active regions (Shimizu et al. 1994). Quiet Sun nanoflares with energies of 10^{24} erg were identified in hard X-rays within polar coronal holes (Koutchmy et al. 1997) and active regions (Hannah et al. 2008; Warmuth & Mann 2020; Battaglia et al. 2021; Fletcher et al. 2011).

The released energy is widely thought to originate from the magnetic field through the sudden dissipation of current sheets within twisted loops (see e.g., Démoulin et al. 1996). Magnetic reconnection occurs in both the corona and the chromosphere/transition region (e.g., Syrovatskii 1971; Litvinenko 1999), and a direct relationship has been established between the magnetic field and the heat input (Rosner et al. 1978; Golub et al. 1980; Serio et al. 1981). The high temperature of the solar corona is sustained by a continuous heat input of approximately 3×10^5 ergs cm^{-2} s^{-1} (Withbroe & Noyes 1977). Parker (1988a) proposed that the dissipation of unresolved current sheets could provide this heating, coining the term "nanoflares" for events with a minimal expected energy of 6×10^{24} ergs per event in an entire active region loop. The corona might then be powered by numerous small-scale current sheets that dissipate in clusters (see also Gold 1964; Petschek 1964; Syrovatskii 1971; Parker 1972; Priest 1981; Priest et al. 1998; Klimchuk 2015, 2006), though their typical energy was below the sensitivity threshold of earlier instruments (Golub & Pasachoff 2010).

⋆ Corresponding author: Olena Podladchikova e-mail: epodlada@gmail.com

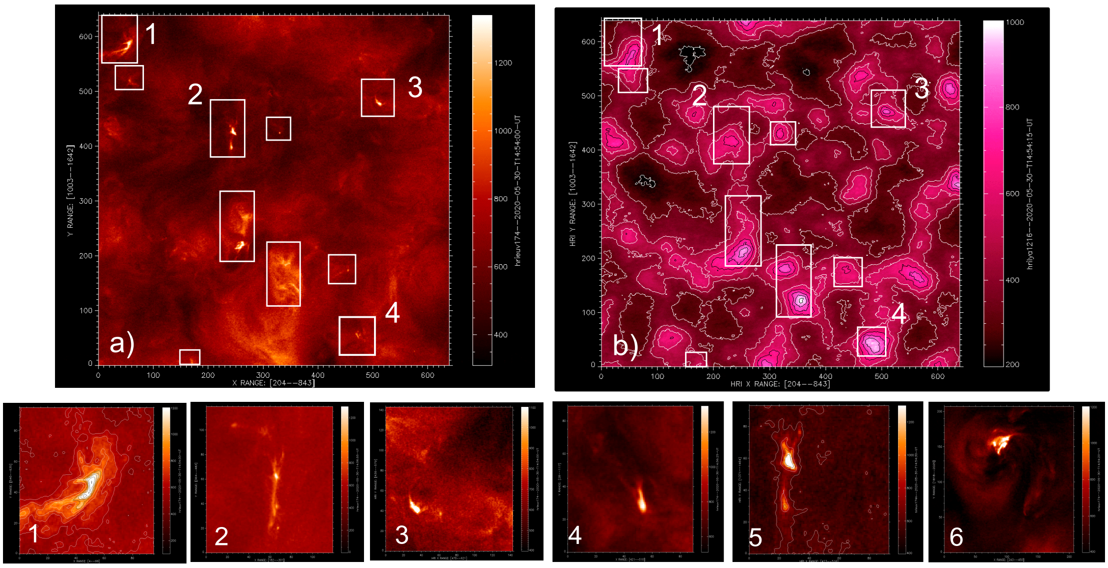

Fig. 1. Previously unresolved solar structures observed by Solar Orbiter $\mathrm{HRI_{EUV}}$ 174 Å campfires on May 30, 2020 at the quiet sun (QS) while Solar Orbiter was located half-way to the Sun, above the chromospheric network (bright patterns in panel b). The main frame (120 × 120 Mm) shows the context in Lyman-α. The bottom panels (20 × 20 Mm each) highlight specific event types: (1,5) intermittent dissipation along quiet sun QS miniloops; (2) multiple-loop reconnection; (3) single-loop burst initiating at the top; (4) tiny reconnection with plasma ejection; (6) picoflare at loop base. Dynamic views are available online: (a), (b), (1), (2), (3), (4), (5), (6).

A decade later, systematic observations of smaller-scale flares were obtained with EUV imagers and spectrometers on SOHO and TRACE (Berghmans et al. 1998; Krucker & Benz 1998; Parnell & Jupp 2000; Harra et al. 2000; Aschwanden & Parnell 2002; Benz & Krucker 2002; Verbeeck et al. 2019), revealing impulsive heating events within the energy range of 10^{24} to 10^{26} ergs. The smallest EUV bursts observed by these missions and subsequent ones like SDO/AIA (Joulin et al. 2016; Ulyanov et al. 2019; Chitta et al. 2021; Purkhart & Veronig 2022) and Hi-C (Subramanian et al. 2018) were on the order of $\approx 10^{24}$ ergs. This raised an intriguing question: about whether even smaller flares with energies as low as 10^{21} ergs could be observed. Aschwanden et al. (1999) extrapolated flare characteristics to estimate a minimal observable energy of 2×10^{24} ergs for a 700 km, 1 MK loop, defining the nanoflare threshold. Recently, Ulyanov et al. (2019) reported nanoflares of $\approx 10^{23}$ erg and predicted the existence of $\approx 10^{21}$ erg flares from currents dissipating in loops as short as 300 km. This aligns with Parker (1988b)'s prediction of collective "topological dissipations" and the theoretical work of Einaudi & Velli (1994), which suggested the thermal energy from an elementary current sheet could be as low as 3×10^{16} ergs.

Furthermore, radio observations of noise storms have revealed small electron acceleration episodes with energies of 10^{20}–10^{24} erg (James & Subramanian 2018; James et al. 2017), comparable to the picoflare energy range investigated here. Recent Solar Orbiter observations have also identified picoflare jets in coronal holes that contribute to solar wind generation (Chitta et al. 2023, 2025), establishing the broader significance of small-scale energy releases in coronal heating and wind acceleration.

The number of detected small-scale events has consistently increased with improvements in instrumental sensitivity, spatial resolution, and temporal resolution. EUV instrumentation has revealed numerous nanoflares, characterized by densities of $n_e = (0.2\text{–}2) \times 10^9\ \mathrm{cm^{-3}}$, temperatures of 1–2 MK, spatial scales of 10–100 Mm, and durations of 0.5–10 minutes. The discovery of these EUV nanoflares has identified a previously missing energy source for coronal heating, underscoring the need to investigate these additional mechanisms to explain the corona's anomalously high temperature.

The High-Resolution Imager ($\mathrm{HRI_{EUV}}$) of the EUI instrument (Rochus & et al. 2019) aboard Solar Orbiter (Müller et al. 2019) observed the quiet corona during deep solar minimum with a cadence of a few seconds, revealing even smaller EUV brightenings than nanoflares. Termed "campfires" due to their prolonged appearance, these events emitted in the 174 Å coronal channel. Their spatiotemporal characteristics, emission measure, and temperature are detailed in Berghmans et al. (2021). Utilizing Solar Orbiter's unique vantage point, Zhukov et al. (2021) performed stereoscopic triangulation to determine that weaker events were situated $1\text{–}2.5\times10^3$ km above the photosphere, while larger ones occupied a narrow vertical layer at $2.5\text{–}5 \times 10^3$ km, where the plasma $\beta \ll 1$ (Gary 2001). This strongly suggests the energy releases observed by $\mathrm{HRI_{EUV}}$ are produced by field-aligned current sheets along coronal loops near the transition region (see Demoulin & Klein (2000)).

The historical progression of flare detection sensitivity reveals a remarkable trend: each generation of instrumentation has revealed increasingly numerous small-scale energy releases. Early hard X-ray observations in the 1980s detected events at rates of $\sim 10^{-25}\ \mathrm{s^{-1}\ cm^{-2}}$, while 1990s-2000s EUV telescopes improved this to $\sim 10^{-22}\text{–}10^{-21}\ \mathrm{s^{-1}\ cm^{-2}}$. The recent $\mathrm{HRI_{EUV}}$ observations continue this progression, pushing detection limits to previously inaccessible energy regimes and revealing the true density of small-scale heating events predicted by Parker's nanoflare hypothesis.

This work continues the analysis of the campfire events discovered by Berghmans et al. (2021), who provided the first observations and characterization of these events, including their detection methodology and preliminary statistics. Building upon their work and the stereoscopic height determinations by Zhukov et al. (2021), we extend the analysis to provide complete energy distributions and occurrence rates. Here, we classify these same events, quantify their energy distribution through power-law analysis using the emission measure and temperature parameters established in the original study, and assess their contribution to coronal heating, integrating picoflares into the general picture of solar atmospheric energy balance.

2. First Observations and Measurements of EUV Campfires

2.1. Observational Setup and Data Acquisition

We build upon the initial discovery and catalog of solar "campfires" by Berghmans et al. (2021). These flare-like events, detected by the High-Resolution Imager (HRI_{EUV}) on Solar Orbiter, were previously characterized by their geometrical properties and basic thermodynamic parameters (emission measure, temperature, length, width). The goal of this study is a comprehensive, detailed analysis of their thermal energy. The analysis uses the same set of observations from May 30, 2020, during deep solar minimum: a sequence of 50 calibrated images in the 174 Å passband from 14:54:00 to 14:58:05 UT at a 5 second cadence.

The HRI_{EUV} telescope, with its 2048×2048 pixel array, imaged a $17' \times 17'$ quiet Sun region. At Solar Orbiter's perihelion (0.556 AU), the two-pixel angular resolution of 1 arcsecond corresponds to a spatial footprint of 198 km on the Sun. This represents a significant improvement over previous 1 AU observations, enabling detection of previously unresolved small-scale events. Future observations from closer perihelia (0.3 AU) will further improve the spatial resolution to approximately 100 km, advancing toward fundamental scales of coronal structures.

During these observations, Solar Orbiter was positioned 31.5° west of Earth, enabling stereoscopic determination of event heights and vertical extents through triangulation with SDO/AIA (Zhukov et al. 2021).

2.2. Event Detection and Classification Methodology

We employ the same event sample and automated detection method using wavelet transforms as described in Berghmans et al. (2021). Events were identified as local brightness enhancements exceeding a $5\sigma/3\sigma$ threshold above the background noise, lasting more than one frame and spanning more than one pixel. Our analysis confirms and extends their event statistics while providing the missing power-law indices for the energy distribution.

Two detection thresholds were applied to sample the event population:

- $\geq 5\sigma$ threshold: 1,467 events (primary analysis sample) with occurrence rate of 3.3×10^{-21} s^{-1} cm^{-2}
- $\geq 3\sigma$ threshold: 12,107 events (extended sample including weaker events) with occurrence rate of 2.7×10^{-20} s^{-1} cm^{-2}

These occurrence rates continue the historical trend of increasing small-scale event detection with improving instrumentation, representing a factor of ~60 increase over previous quiet Sun studies and approximately five orders of magnitude higher than early hard X-ray observations (Lin et al. 1984).

The full-Sun occurrence rates for these event samples are:

- $\geq 5\sigma$ events: 62 events per second (full-disk equivalent)
- $\geq 3\sigma$ events: 518 events per second (full-disk equivalent)

Event durations ranged from 1-260 s, with the longest events approaching 200 seconds. The total observation duration of 260 s necessarily truncates some events at the sequence boundaries.

2.3. Morphological Classification

This analysis focuses on small-scale miniloops in the quiet-Sun EUV corona, as observed from a near-Sun vantage point. Visual inspection and event detection revealed four distinct morphological types of campfires.

- **Multi-miniloop reconnecting events with mass ejection**: Exhibiting complex magnetic reconnection between multiple loop systems (Priest & Forbes 2000)
- **Single partial-miniloop sudden heating events**: Characterized by brightening primarily around the loop tops (Krucker & Benz 2000)
- **Single full-miniloop sudden heating events**: Consistent with turbulent reconnection of multiple small-scale current sheets throughout the loop structure (Priest et al. 1998; Cargill & Klimchuk 2004; Browning & Van der Linden 2003).
- **Single-dot heating events**: Compact events of approximately 200 km linear size, whose detailed structure remains to be resolved with future instrumentation

Intermittent dynamic brightenings along miniloop structures were frequently observed, with high-cadence HRI_{EUV} observations sometimes resolving the rapid sequential heating of different quiet sun miniloop segments. This morphological diversity provides a robust observational basis for testing coronal heating models.

All detected campfires were co-identified in simultaneous SDO/AIA observations, though they appear more blurred due to AIA's lower spatial resolution. This cross-instrument identification, detailed in Paper I (Berghmans et al. 2021), enables the application of well-established DEM analysis techniques developed for SDO data.

3. Thermal Energy in Optically Thin Coronal Plasma

3.1. Thermal Energy Framework

For EUV brightening events identified in solar corona observations, we calculate their thermal energy using established methodologies for optically thin plasma (Benz & Krucker 1998). The thermal energy is defined as:

$$E_{th} = 3n_e k_B T V$$

where n_e is the electron density, T is the temperature, k_B is Boltzmann's constant, and V is the volume of the brightened region.

The primary challenge in coronal energetics lies in determining the true three-dimensional volume from two-dimensional projections in optically thin emission. We address this through multiple volume models and uncertainty quantification, as detailed below.

3.2. Geometrical Parameters and Volume Models

We analyze the same event sample as Berghmans et al. (2021), applying elliptical fitting to determine geometric parameters while extending the analysis to include weaker ($\geq 3\sigma$) events. For each campfire, the projected event region was fitted with an encompassing ellipse using Python's least-squares minimization routine, deriving:

- Length (major axis): $L \approx 0.198$ to 3.8 Mm
- Width (minor axis): $w \approx 0.198$ to 2.65 Mm

- Duration: 1 to 260 seconds

Error analysis reveals increasing relative uncertainties for the smallest events near the detection threshold, ranging from 1% for the largest dimensions to 8.3% for the smallest dimensions. This reflects the fundamental challenge of measuring sub-resolution features, where the two-pixel spatial resolution of 198 km establishes the minimum detectable scale. These measured parameters are consistent with the methodology and range reported in Berghmans et al. (2021) for the $\geq 5\sigma$ events, while our extended analysis includes additional weaker events with correspondingly larger relative uncertainties.

Event areas were calculated using the standard elliptical area formula $A = \pi(L/2)(w/2)$, yielding $A \approx 0.031$ to 7.9 Mm^2.

To assess the robustness of our energy estimates against geometrical assumptions, we employed three distinct volume models:

1. **Elliptical loop model**: Based on loop geometry following Aschwanden et al. (2000), providing the most physically realistic estimates
2. **Cube model A**: $V = L \cdot w \cdot h$ with $h = \sqrt{A}$, where A is the event area
3. **Cube model B**: $V = L \cdot w \cdot h$ with $h = 1000$ km

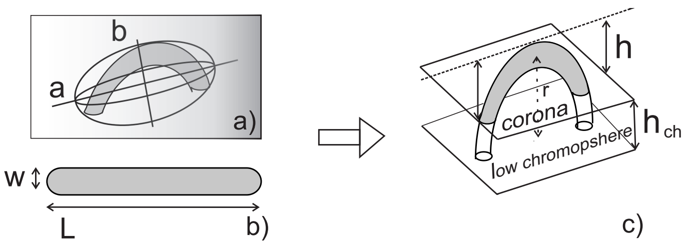

Fig. 2. Aschwanden et al. (2000) EUV brightening volume modelling as an elliptical loop model. $\mathrm{HRI_{EUV}}$ flaring loops are observed in the low corona, chromospheric segments are truncated $h_{ch} = 500$ km from the brightening of the coronal EUV volume. (a) The ellipsoidal axes a and b confine the geometry of the projected loop, from which the projected loop length L and width w can be determined in (b) and (c).

For the elliptical loop volume model, which shows the best agreement with stereoscopic measurements (Zhukov et al. 2021), the volume of the brightened part of the loops is calculated as:

$$V_{EUV} = V_{loop}\left[1 - \frac{2}{\pi}\arctan\left(\frac{h_{ch}}{L/2}\right)\right]$$

where the full loop volume is:

$$V_{loop} = \frac{\pi^2 r w^2}{4}, \quad r = \sqrt{(L/2)^2 + h_{ch}^2} - w/2$$

Volume Ranges: The resulting volume ranges are:

- Elliptical model: $V_{\mathrm{EUV}} \approx 0.005$ to 9.3 Mm^3
- Cube model A: $V \approx 0.008$ to 10.1 Mm^3
- Cube model B: $V \approx 0.039$ to 10.1 Mm^3

The smallest detectable area of ≈ 0.031 Mm^2 corresponds to the fundamental resolution limit for an ellipse with $L = w = 0.198$ Mm, while the maximum area represents the largest elliptical regions detected. This multi-model approach allows us to assess the robustness of our energy estimates against volume assumptions, as demonstrated in previous EUV nanoflare studies (Ulyanov et al. 2019; Aschwanden et al. 2000).

3.3. Temperature Determination via DEM Analysis

The emission measure-weighted temperature (T) and total emission measure (EM) for each campfire were determined in Berghmans et al. (2021) using differential emission measure (DEM) analysis applied to co-aligned SDO/AIA coronal channels, following Hannah & Kontar (2012). This methodology, extensively validated in previous studies and detailed in Paper I Berghmans et al. (2021), derives both total emission measure (temperature-integrated) and EM-weighted temperature (Parenti et al. 2017) for each pixel and campfire.

While the fundamental DEM, EM, and T parameters for the events analyzed here were established in Berghmans et al. (2021), we provide additional discussion and validation analysis of these measurements in the context of our energy calculations.

The DEM analysis provides robust temperature estimates by leveraging the temperature response functions of multiple EUV passbands, ensuring accurate determination of this critical parameter for thermal energy calculations.

3.4. Electron Density Determination

The electron density (n_e) is derived from the emission measure (EM) through the fundamental relationship for optically thin plasma:

$$EM = n_e^2 \cdot V$$

We employed two complementary approaches for density determination:

1. DEM Analysis Method: Using the Hannah & Kontar DEM inversion technique applied to SDO/AIA coronal channels, we obtain the total emission measure for each campfire. The electron density is then calculated as:

$$n_e = \sqrt{\frac{EM}{V}}$$

where V is derived from the geometrical models described above.

2. Filter Ratio Method: For events with sufficient signal-to-noise ratio in multiple EUV passbands, we apply the filter-ratio technique following Aschwanden et al. (2000), which provides an independent estimate through:

$$n_e = \sqrt{\frac{EM}{w}}$$

where w is the loop width measured from elliptical fitting.

3.5. Method Validation and Parameter Consistency

The consistency of physical parameters derived through independent methods validates our approach. Both DEM analysis and filter-ratio techniques yield comparable results for temperature and density, with electron densities in the range of $n_e \approx 10^8$–10^9 cm^{-3} for $\mathrm{HRI_{EUV}}$ campfires, typical for quiet Sun coronal structures.

The DEM method provides more reliable results for weaker events, while the filter-ratio method offers better temperature discrimination for brighter events. The obtained densities and temperatures are comparable to those reported for TRACE nanoflares (Aschwanden et al. 2000) and SDO/AIA microflares (Ulyanov et al. 2019), confirming that campfires represent a continuation of the flare energy distribution to smaller scales.

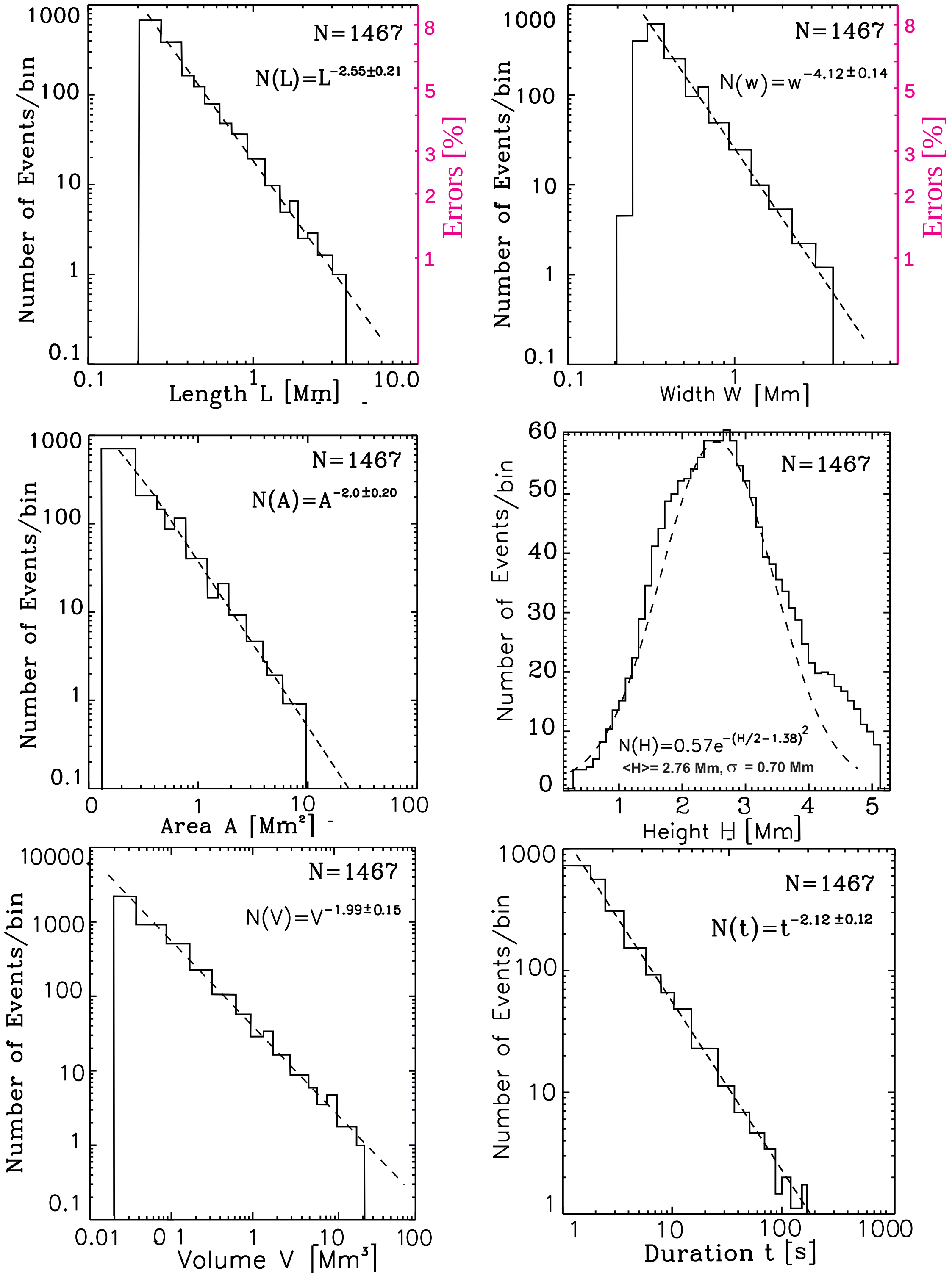

Fig. 3. Distributions of HRI_{EUV} campfire parameters derived through elliptical fitting: length L, width w, area A, elliptical loop volume V, duration t, and stereoscopic heights H above the photosphere. Magenta curves show relative measurement errors, highlighting the increasing uncertainties for the smallest events near the detection threshold (1% to 8.3% relative error). The area distribution spans 0.031 to 7.9 Mm^2 (elliptical areas). Comparison with TRACE EUV nanoflare parameters reveals campfire volumes are approximately three orders of magnitude smaller while maintaining consistent physical scaling relationships.

3.6. Uncertainty Quantification and Robustness Analysis

To ensure the reliability of our results, we conducted uncertainty analysis considering multiple factors:

- **Event detection thresholds**: Comparison of $\geq 3\sigma$ versus $\geq 5\sigma$ samples shows consistent occurrence rates with Berghmans et al. (2021)
- **Volume model assumptions**: Three different geometrical models yield consistent power-law behavior

- **DEM inversion uncertainties**: Mean statistical error of 2% in EM has minimal impact on distribution slopes
- **Temperature determination**: Errors <10% for quiet Sun conditions are within acceptable ranges
- **Geometrical parameter measurement**: Quantified errors in length/width measurements (1-8.3%) do not affect main conclusions
- **Statistical significance**: Large sample sizes (1,467–12,107 events) ensure statistical robustness

Our analysis demonstrates that while absolute energy values show some model dependence, the power-law character of the energy distribution remains robust across all uncertainty sources. The consistency between different methodological approaches validates our main conclusions.

4. From Campfires to Picoflares: Energy Classification and Heating Contribution

4.1. Geometrical Parameters of Campfires

We determined geometric parameters through elliptical fitting of projected event regions using Python's least-squares minimization routine. Length (L) and width (w) were derived from the ellipse's major and minor axes, with rigorous error quantification showing relative errors from 1% for largest dimensions to 8.3% for smallest dimensions.

The analysis reveals compact event morphology:

- Length: $L \approx 0.198$ to 3.8 Mm
- Width: $w \approx 0.198$ to 2.65 Mm
- Area: $A \approx 0.039$ to 10 Mm^2
- Volume: $V_{EUV} \approx 0.009$ to 11 Mm^3
- Duration: 1 to 260 seconds

These parameters are substantially smaller than EUV nanoflares (Aschwanden et al. 2000), with linear dimensions approximately an order of magnitude smaller and volumes about three orders of magnitude smaller. Errors in length and width definition range from 1% for the largest dimensions (2.65-3.8 Mm) to 8.3% for the smallest dimensions (0.198 Mm).

While our area distribution shows some differences in shape and range compared to Berghmans et al. (2021), this reflects our extended analysis including weaker ($\geq 3\sigma$) events and refined elliptical fitting methodology. The consistent power-law character across both studies confirms the robustness of the underlying distribution.

4.2. Stereoscopic Determination of Height above the Photosphere

Stereoscopic analysis by Zhukov et al. (2021) of campfire events discovered by Berghmans et al. (2021) provides the first direct measurement of their vertical distribution (Fig. 4), revealing concentrations at altitudes of $H \approx 1 - 5$ Mm (mean $\langle H \rangle = 2.76$ Mm, $\sigma = 0.70$ Mm). This low-altitude concentration challenges existing theoretical models and suggests energy releases from field-aligned current sheets along coronal loops near the transition region, which constitutes a relatively thin layer in the upper chromosphere/low corona.

The measured heights are substantially lower than the $H \approx 100-200$ Mm predicted by standard reconnection models (Priest & Forbes 2000; Demoulin & Klein 2000), indicating that theoretical mechanisms must account for additional magnetic energy dissipation processes.

While this geometric parameter characterizes only the vertical extent rather than thermal energy content, it provides crucial constraints on the physical mechanisms involved. We emphasize these pioneering stereoscopic measurements and their implications for understanding coronal heating processes in our Discussion.

4.3. Temperature, Emission Measure, and Comparison with X-ray Flares

We present the emission measure-weighted temperature (T) and total emission measure (EM) for 1,467 ($> 5\sigma$) HRI$_{\rm EUV}$ campfires as established and determined with their thermodynamic parameters in Berghmans et al. (2021), who applied differential emission measure (DEM) analysis to co-aligned SDO/AIA coronal channels following Hannah & Kontar (2012). Event temperatures peak at $\log T \approx 6.1$ ($\sim$ 1.3 MK) compared to the background peak at $\log T \approx 6.0$ ($\sim$ 1.0 MK), and event emission measures are roughly an order of magnitude higher. We use these established parameters to calculate thermal energies and place the events in the broader context of solar flare energetics.

For context and to demonstrate the relative proportions of these events, we compare these parameters with typical X-ray flare values. The emission measure-temperature relationship for HRI$_{\rm EUV}$ campfires (0.97 – 3.5 MK range) follows:

$$EM = 10^{36.50} \times T^{1.90\pm0.35}$$

This relationship (Fig. 5) is consistent with multi-instrumental energy characteristics of solar flares and microflares, but occurs at lower coronal temperatures. The comparison reveals that campfires would correspond to GOES classes at least three orders of magnitude lower than those observed in X-rays, highlighting their distinctly smaller energy scale.

4.4. Thermal Energy Distribution and Statistical Characteristics

The 1,467 campfires detected in Paper I above the 5σ brightness threshold exhibit thermal energies ranging from 9.1×10^{20} to 9.8×10^{23} erg for the elliptical loop volume model. We found that the flare volume values derived from different geometric models do not significantly influence the resulting thermal energy estimates. The choice of volume model affects the absolute energy values but preserves the overall distribution characteristics.

The frequency distribution (Fig. 6a) spans over three orders of magnitude in energy and is well-described by a power-law function with index -2.32 ± 0.35 as determined by maximum likelihood estimation. While power-law behavior provides the best statistical fit and maintains continuity with established flare energy distributions, we note that alternative functional forms (exponential, log-normal) cannot be definitively excluded given the current data range and sample size.

When including events above the 3σ threshold (12,107 events), the thermal energy range extends downward to 3.4×10^{20} erg (Fig. 6b). This expanded sample reveals a steeper distribution with power-law index -2.74 ± 0.23, indicating a substantial population of lower-energy events. The increased statistical power of this larger sample strengthens the evidence for scale-free behavior in the campfire energy distribution.

The elliptical model provides the most physically realistic estimates, supported by stereoscopic validation (Zhukov et al. 2021). The statistical characteristics of campfire energies show remarkable consistency with the scaling behavior observed in

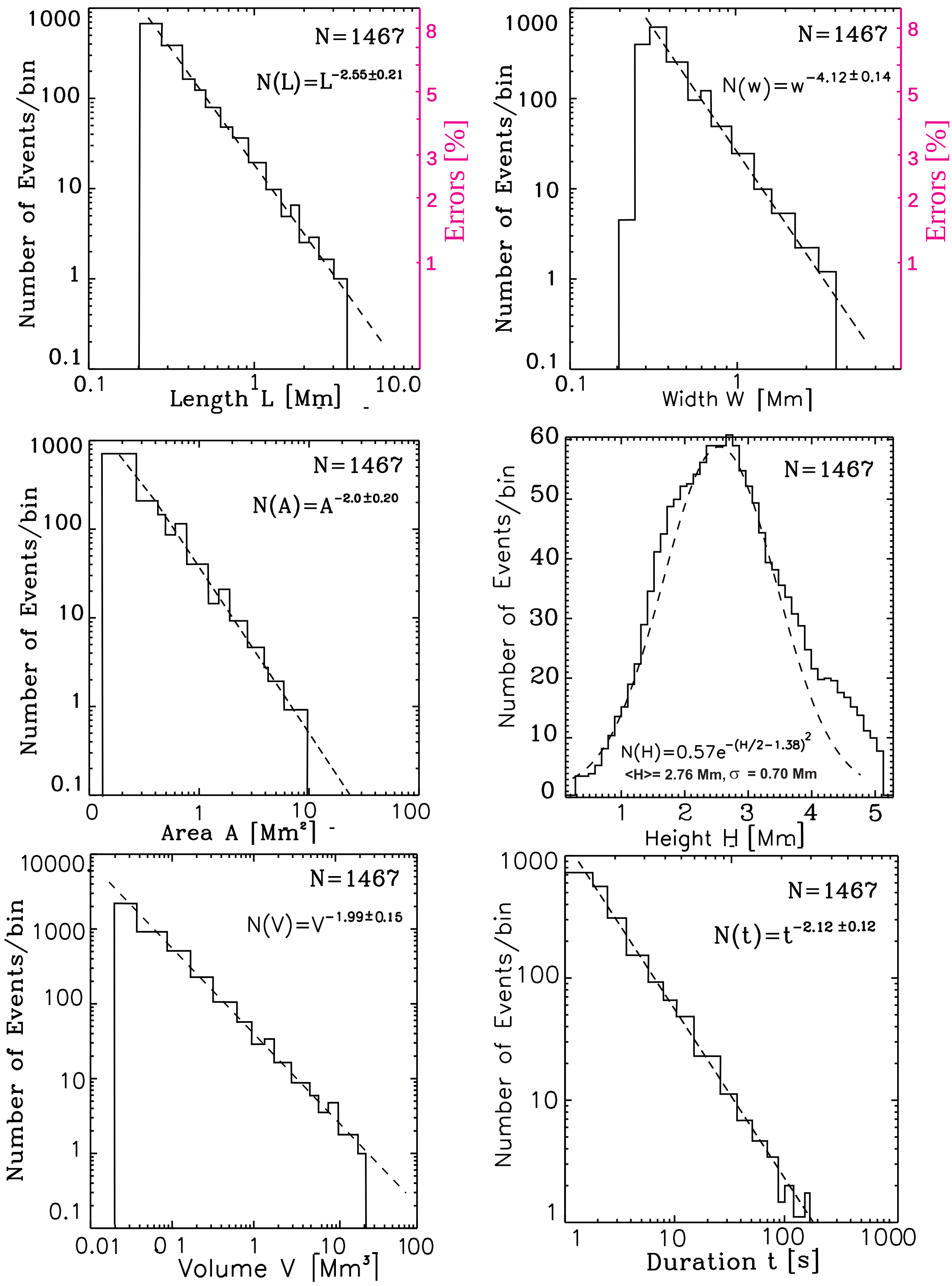

Fig. 4. Power-law distributions of HRI_{EUV} campfire parameters: length L, width w, area A, elliptical loop volume V, duration t, and heights H above the photosphere. Magenta curves show relative errors in length and width estimation, ranging from 1% for largest dimensions (2.65-3.8 Mm) to 8.3% for smallest dimensions (0.198 Mm). Comparison with TRACE EUV nanoflare parameters (Fig. 4 in Aschwanden et al. (2000), Fig. 11 in Aschwanden et al. (2016)) reveals campfire volumes are approximately three orders of magnitude smaller.

larger solar flares, supporting their interpretation as the low-energy extension of the flare family.

The power-law distribution of the campfires' geometric parameters is consistent with a turbulent regime, in the sense that magnetic energy dissipation in turbulence follows the scaling laws described in Priest et al. (2002).

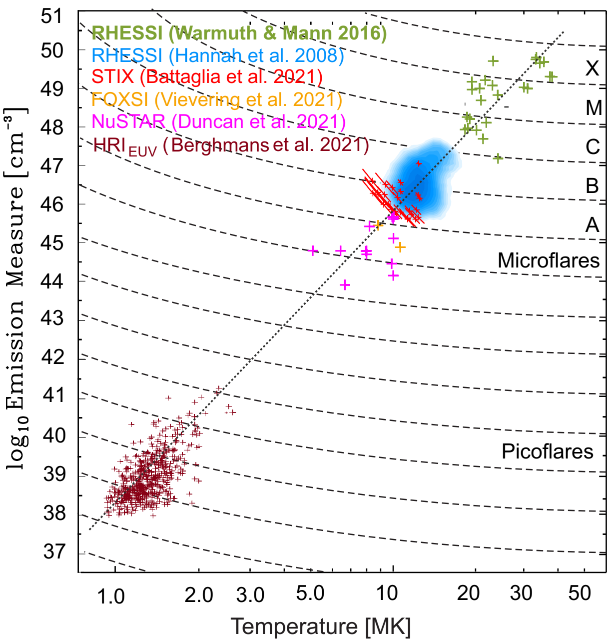

Fig. 5. Emission measure-temperature relationship for the 1,467 $\mathrm{HRI_{EUV}}$ campfire events ($> 5\sigma$) analyzed in this work, using the thermodynamic parameters (emission measure and temperature) established by Berghmans et al. (2021). We compare $\mathrm{HRI_{EUV}}$ emission measures and temperatures with those of X-ray microflares and flares. The relation for $\mathrm{HRI_{EUV}}$ and X-Ray covering the temperature range 0.97 – 3.5 MK follows $EM = 10^{36.50} \times T^{1.90\pm0.35}$. Campfires would correspond to GOES class flares at least three orders of magnitude lower than those observed in X-rays.

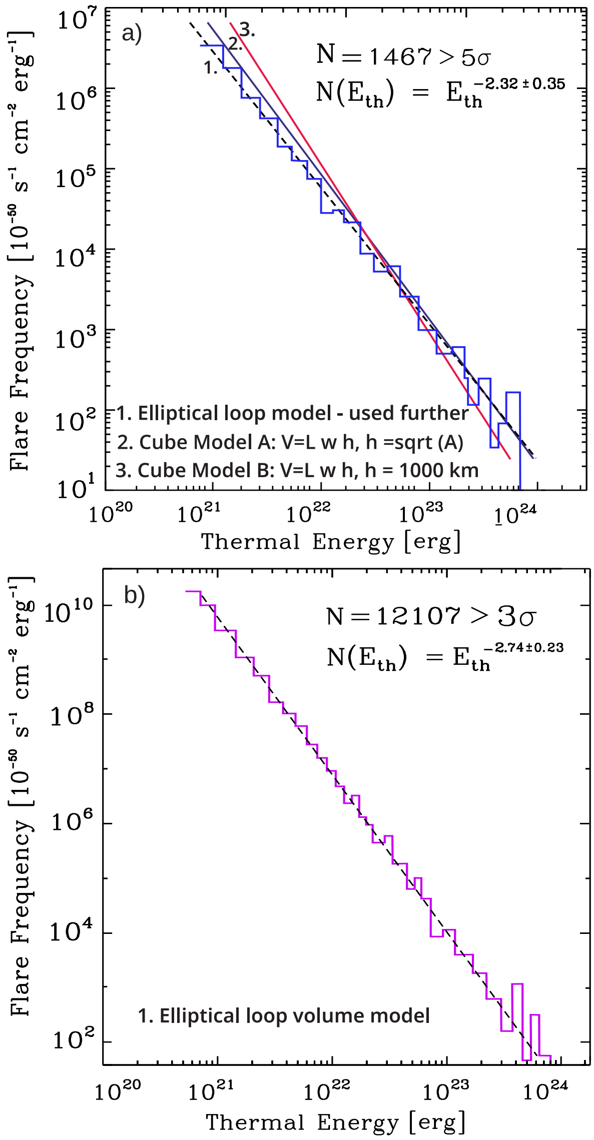

Fig. 6. (a) Volume dependence study of frequency distribution of thermal energies for 1,467 $\mathrm{HRI_{EUV}}$ campfires ($\geq 5\sigma$). The distribution is well-fit by a power law with slope $\alpha = 2.32 \pm 0.35$ (elliptical loop volume model). (b) Distribution for 12,107 campfires ($\geq 3\sigma$ threshold) showing extended dynamic range with power-law index $\alpha = 2.74 \pm 0.23$.

4.5. *Comparison with Previous Studies and Energy Continuum*

The power-law frequency distribution of solar flares extends continuously from the most powerful events ($\approx 10^{32}$ erg) down to the picoflare range ($\approx 10^{21}$ erg) observed here (Fig. 7 and Table 1). This comprehensive comparison demonstrates that campfires represent the low-energy extension of a continuous energy distribution spanning over 15 orders of magnitude, as summarized in Table 1.

While previous studies reported some events in the picoflare energy range (Joulin et al. 2016; Ulyanov et al. 2019), our continuation of the Berghmans et al. (2021) data analysis provides significantly better statistics due to $\mathrm{HRI_{EUV}}$'s superior spatial resolution and near-Sun vantage point. The increased sensitivity reveals a steeper power-law slope for the lower-energy events.

The detected $\mathrm{HRI_{EUV}}$ picoflares ($\geq 3\sigma$ detection) contribute approximately 1% of the additional power required to heat the quiet solar corona (Fig. 7). These observations during deep solar minimum expand the known distribution of solar flares to higher frequencies and lower energies, confirming the existence of a continuum of heating events spanning multiple orders of magnitude. This continuum is comprehensively documented in Table 1, which compares power-law indices and occurrence rates across multiple studies and instrumentation eras.

This continuum is further illustrated in Fig. 8, which shows micro- and nanoflare observation periods from various studies overlaid on the solar activity cycle. The differences in power-law slopes and energy cutoffs visible in both Fig. 7 and Table 1 may be related to the activity level during observations and instrument sensitivity, highlighting the importance of consistent detection thresholds when comparing flare statistics across different studies and solar conditions.

4.6. *Detailed Heating Contribution Analysis and Theoretical Implications*

The cumulative thermal energy input by picoflares provides crucial insights into their role in coronal heating. Summing the thermal energy of all 12,701 $\geq 3\sigma$ picoflares and dividing by the total observing time and area, we obtain an average input power per unit area of $P_{\mathrm{in}} \approx 3.0 \times 10^3$ erg s^{-1} cm^{-2}.

Comparing this with the quiet Sun corona's combined radiative and conductive losses of $P_{\mathrm{out}} \approx 3 \times 10^5$ erg s^{-1} cm^{-2} (Withbroe & Noyes 1977), we find that the observed picoflares contribute approximately 1% of the power required to maintain the quiet corona.

If the power-law distribution $N(E_{\mathrm{th}}) \propto E_{\mathrm{th}}^{-\alpha}$ continues to lower energies with the observed slope ($\alpha = 2.74$), we can esti-

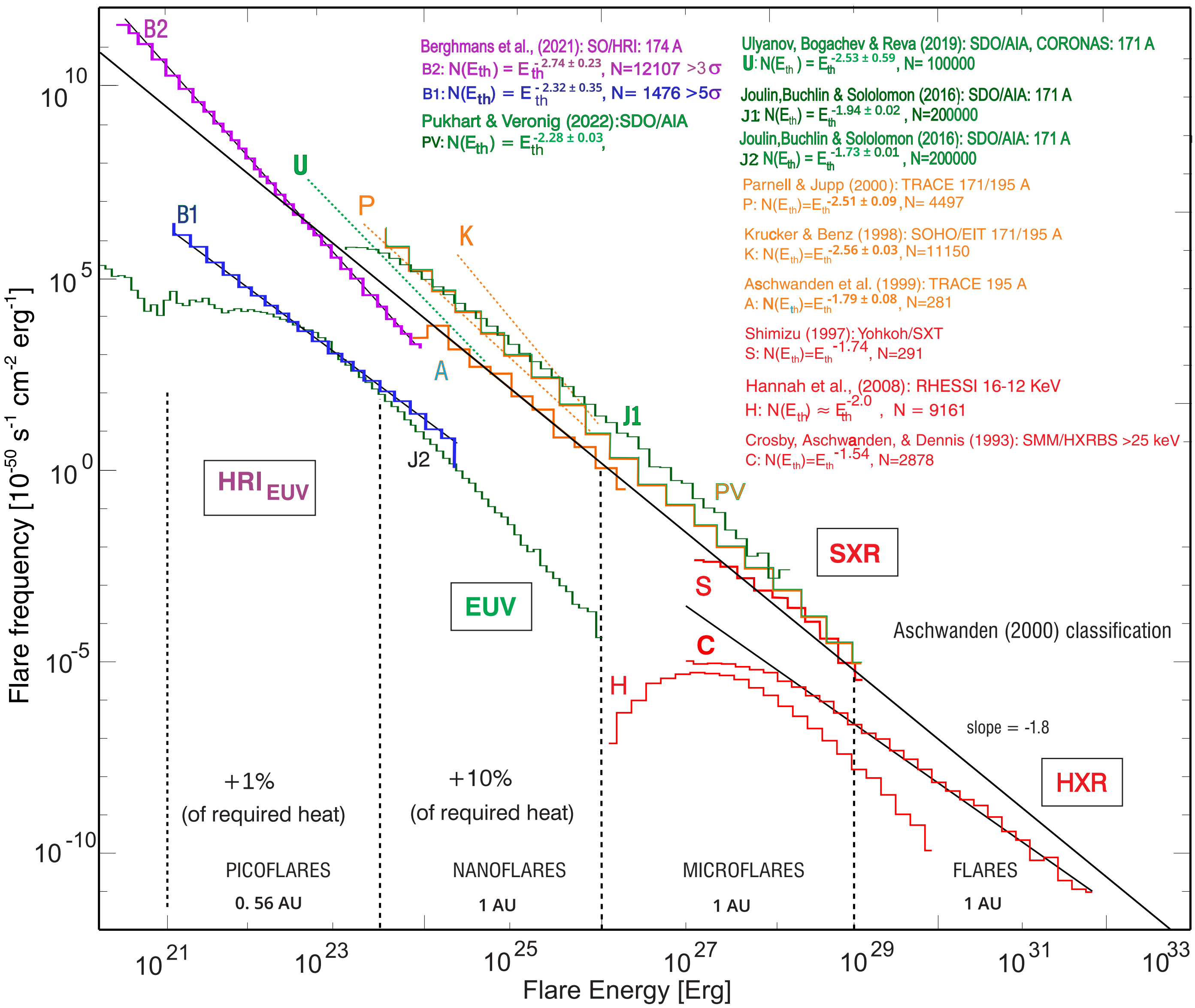

Fig. 7. Frequency distributions of thermal energy of flares observed from 10^{21} erg to 10^{32} erg, detected in hard X-ray, soft X-ray, and EUV in the solar corona. Flare energy distribution can be approximated by power-law functions throughout the entire observed range. Solar Orbiter/EUI campfires observed by the high-resolution EUV imager halfway to the Sun extend toward higher frequencies and lower energies, approaching the fundamental limit of flare-like event detection and contributing approximately 1% of the total energy budget **required** to maintain the solar corona. The red histogram B1 corresponds to thermal energy of 1,467 events ($\geq 5\sigma$) campfires with power-law index $\alpha = 2.32 \pm 0.35$, B2 to 12,107 campfires ($\geq 3\sigma$) with power-law index $\alpha = 2.74 \pm 0.23$.

mate how far the distribution would need to extend for picoflares to supply the remaining heating power:

$$E'_{\rm min} = E_{\rm min} \left(\frac{P_{\rm out}}{P_{\rm in}} \right)^{\frac{1}{\alpha-2}}$$

where $E_{\rm min} = 3.4 \times 10^{20}$ erg is the current detection limit. This calculation reveals that the observed power law would need to continue down to approximately 1.25×10^{18} erg per event for picoflares to completely power the quiet-Sun corona.

This energy scale aligns remarkably well with theoretical predictions. Einaudi & Velli (1999) predicted that $\sim 10^{16}$ erg heating events might be observable in the quiescent corona when Solar Orbiter reaches its closest approach (~0.3 AU). Our continuation confirms that the power-law distribution extends to within two orders of magnitude of this prediction.

The small spatial scales of campfires also have important theoretical implications. For quiet Sun parameters ($B \approx 20$ G, $B_p \approx 2$ G, $q \approx 0.2$), releasing $\sim 10^{21}$ erg requires loop sizes on the order of $L \approx 400$ km, consistent with our observations. This supports Parker's nanoflare model where magnetic energy release returns loops to their potential state.

The timescales also favor certain heating mechanisms. For HRI_{EUV} loop lengths of $10^4 10^5$ km and assuming an Alfvén speed $V_A \approx 1000$ km s^{-1}, we have $t_A \approx 10100$ s, compared to granular convection times $t_p \approx 400900$ s. This favors continuous current dissipation mechanisms over wave heating for quiet solar corona regions.

Table 1. Power-law fits to frequency distributions of thermal energy in flares and nanoflares reported in the literature. Occurrence rates are given both as primary rates (per second per square centimeter) and extrapolated to the entire Sun (both hemispheres). For this work, rates are calculated from event counts observed in a 17′ × 17′ FOV over 260 s, scaled to full spherical Sun equivalent (both hemispheres). Abbreviations: Reg. - Region, Dst. - Distance, En. r. - Energy Range, No. - Number, Ev. - Events, Cd. - Cadence, Rt. - Rate, Ind. - Power-law Index. This work extends the statistical analysis of Berghmans et al. (2021) by providing comprehensive power-law indices using maximum likelihood estimation, while maintaining consistent event detection methodology and occurrence rates.

Study	Reg.	Instrument	Band	Dst. (AU)	En. r. (erg)	No. Ev.(∼)	Cd. (s)	Rt. (s^{-1} cm^{-2})	Rt. (s^{-1})	Ind. α
Active Region (AR) Studies										
Crosby et al. (1993)	AR	SMM/HXRBS	X-ray	1.00	$10^{28}10^{32}$	3×10^{4}	–	2.0×10^{-27}	1.2×10^{-4}	1.54
Verbeeck et al. (2019)	AR	GOES/XRS	X-ray	1.00	10^{28}–10^{32}	9601	–	1.1×10^{-27}	9.2×10^{-6}	1.89
Hannah et al. (2008)	AR	RHESSI	X-ray	1.00	$10^{26}10^{30}$	10^{4}	–	2.1×10^{-27}	1.3×10^{-4}	2.0
Shimizu & Tsuneta (1997)	AR	Yohkoh/SXT	X-ray	1.00	$10^{25}10^{30}$	$>10^{4}$	24	1.1×10^{-21}	67	1.74
Quiet Sun (QS) Studies										
Lin et al. (1984)	QS	Balloon HXR	X-ray	1.00	$10^{24}10^{27}$	138	–	2.1×10^{-25}	1.3×10^{-2}	–
Berghmans et al. (1998)	QS	SOHO/EIT	EUV	0.99	$10^{24}10^{27}$	10^{4}	66	4.3×10^{-22}	26	2.0
Aschwanden et al. (2000)	QS	TRACE	EUV	1.00	$10^{24}10^{26}$	281	125	1.3×10^{-22}	8	1.79
Aschwanden & Parnell (2002)	QS	TRACE	EUV	1.00	$10^{25}10^{27}$	5×10^{3}	80	1.8×10^{-22}	11	1.8
Joulin et al. (2016)	QS	SDO/AIA	EUV	1.00	$10^{23}10^{25}$	2×10^{5}	120	3.9×10^{-22}	48	1.73
Harra et al. (2000)	QS	SOHO/CDS	EUV	0.99	$10^{25}10^{27}$	1.1×10^{3}	15	5.5×10^{-22}	33	1.7
Ulyanov et al. (2019) (TESIS)	QS	TESIS/CORONAS	EUV	1.00	$10^{24}10^{26}$	8.5×10^{4}	4–5	6.1×10^{-21}	370	2.43
Ulyanov et al. (2019) (AIA)	QS	SDO/AIA	EUV	1.00	$10^{23}10^{26}$	2.2×10^{4}	12	6.2×10^{-21}	380	2.18
Purkhart & Veronig (2022)	QS	SDO/AIA	EUV	1.00	$10^{24}10^{29}$	10^{5}	12	3.7×10^{-21}	225	2.28
Berghmans et al. (2021) ($\geq 5\sigma$)	QS	SolO/EUI	EUV	0.556	–	1.5×10^{3}	3–5	3.3×10^{-21}	63	–
- This work ($\geq 5\sigma$)	QS	SolO/EUI	EUV	0.556	$10^{21}10^{24}$	1.5×10^{3}	3–5	3.3×10^{-21}	63	2.32
- This work ($\geq 3\sigma$)	QS	SolO/EUI	EUV	0.556	$10^{21}10^{24}$	1.2×10^{4}	3–5	2.7×10^{-20}	518	2.74
Mixed Region Studies										
Parnell & Jupp (2000)	MIX	TRACE	EUV	1.00	$10^{23}10^{26}$	5×10^{3}	115	9.6×10^{-22}	58	2.4
Benz & Krucker (2002)	MIX	SOHO/EIT	EUV	0.99	$10^{25}10^{27}$	1.1×10^{3}	–	2.1×10^{-27}	0.013	2.3

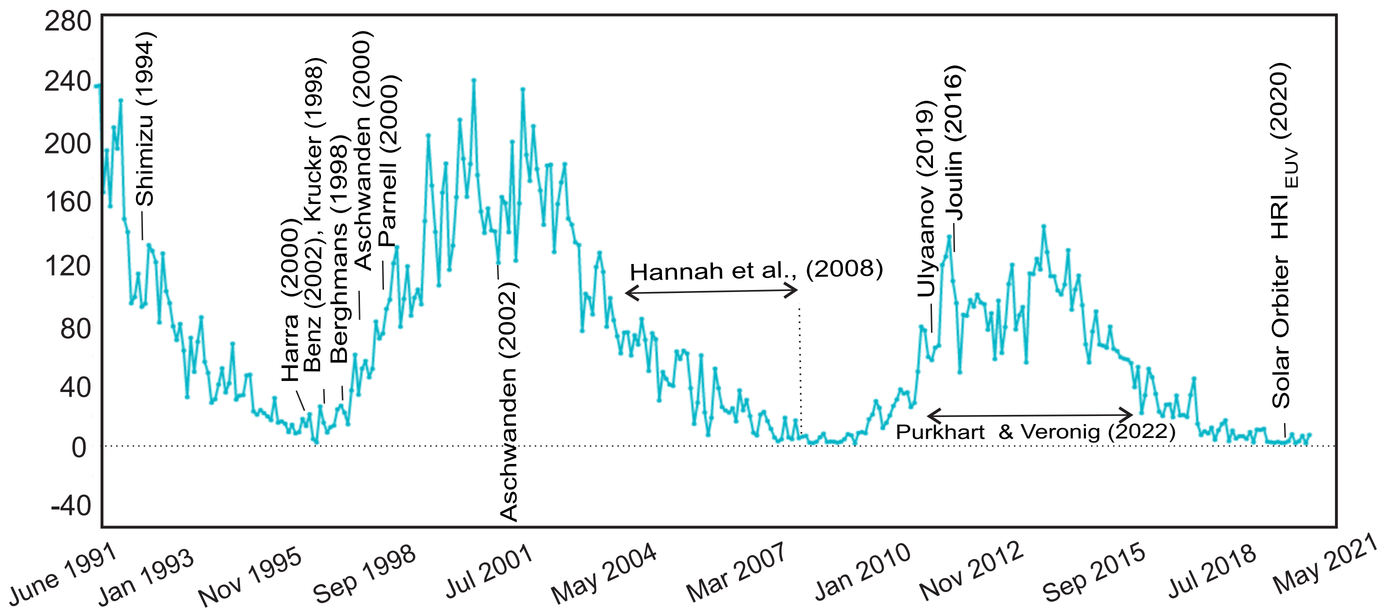

Fig. 8. Micro- and nanoflare observation periods from various studies overlaid on the sunspot number (a proxy for solar activity). Differences in power-law slopes and energy cutoffs may be related to the activity level during observations and instrument sensitivity.

4.7. Robustness of Results and Statistical Significance

As detailed in Section 3.6, our uncertainty analysis confirms the robustness of these findings across multiple methodological variations and potential error sources, including event detection thresholds, volume model assumptions, DEM inversion uncertainties, and statistical significance of large sample sizes.

To ensure reliable detection near the instrumental limit, we excluded candidates occupying only one pixel or one time frame, minimizing false detections. Despite uncertainties in measured and modeled parameters, our analysis indicates that the general trends and power-law behaviors are not significantly affected.

The combination of multiple volume models, detection thresholds, and independent parameter estimation methods confirms that picoflares represent a statistically significant population in the quiet corona. Extending the observation duration or area did not alter the fitted power-law slopes beyond their stated uncertainties, demonstrating the robustness of our main results.

5. Discussion

The thermal energy analysis of the May 30, 2020 Solar Orbiter HRI_{EUV} campfires presented in this work reveals that campfires represent picoflaresthe smallest energy release events yet observed in the solar corona. Their identification as a distinct energy class below traditional nanoflares has significant implications for our understanding of coronal heating mechanisms.

The unique vantage point of Solar Orbiter at 0.556 AU, combined with stereoscopic observations with SDO, has enabled unprecedented resolution of small-scale coronal structures. The stereoscopic determination of event heights by Zhukov et al. (2021) provides crucial independent constraints on plasma parameters in the low corona, offering new opportunities to test and refine heating models.

Our measurements suggest that current theoretical frameworks may need to incorporate additional dissipation mechanisms beyond the well-established perpendicular current models. The observed concentration of picoflares at low coronal altitudes (1-5 Mm) challenges standard reconnection models that typically predict energy release at higher altitudes. This discrepancy indicates that field-aligned (parallel) current dissipation may play a more significant role than previously considered.

5.1. Plasma Beta Conditions and Current Dissipation Regimes

The stereoscopic height measurements by Zhukov et al. (2021) reveal that picoflares concentrate at low altitudes (1-5 Mm) where plasma beta conditions ($\beta \ll 1$) strongly favor field-aligned (parallel) current dissipation over perpendicular reconnection. This represents a significant shift from traditional nanoflare modeling, which typically considered energy release in higher coronal regions where β conditions might support different dissipation mechanisms.

This low plasma beta ($\beta \ll 1$) condition in the 1-5 Mm altitude range indicates magnetic pressure dominance over gas pressure, fundamentally distinguishing the reconnection environment from higher-altitude scenarios where different β regimes may prevail. The consistent low-β conditions across all picoflare heights suggest field-aligned current dissipation as the primary mechanism, unlike larger flares that may occur across multiple β regimes and altitudes.

In the low-β regime characteristic of the observed picoflare altitudes, current dissipation occurs primarily through parallel currents via anomalous resistivity mechanisms. This contrasts with the perpendicular current dissipation through magnetic reconnection that dominates in high-β plasmas. The prevalence of parallel current dissipation in picoflares suggests that current-driven instabilitiessuch as drift waves, ion-acoustic waves, and lower-hybrid wavesmay play a crucial role in converting magnetic energy to heat at these small scales.

5.2. Characteristic Timescales of Current Dissipation

The observed picoflare durations (1-260 s) align with theoretical timescales based on event geometry:

Perpendicular Current Dissipation (Reconnection):

$$\tau_\perp \sim \frac{L}{V_A} \approx \frac{10^3 - 5\times 10^3 \text{ km}}{1000 \text{ km/s}} \approx 1 - 10 \text{ s}$$

where L is the current sheet length and V_A the Alfvén speed.

Parallel Current Dissipation (Anomalous Resistivity):

$$\tau_\parallel \sim \frac{L}{c_S} \approx \frac{10^3 - 5\times 10^3 \text{ km}}{50 - 150 \text{ km/s}} \approx 7 - 100 \text{ s}$$

where c_S is the ion sound speed. This slower dissipation produces more gradual heating events and helps explain the observed duration distribution spanning both rapid (1-10 s) and slower (10-100 s) timescales.

The loop width - fibril width ($w \sim 100 - 200$ km) according to Parker (1988a) determines current sheet thickness and reconnection rates, but the overall event duration is governed by signal propagation at Alfvén speed along the structure length L. This distinction explains why we observe two populations in the duration distribution: rapid impulsive events (1-10 s) characteristic of perpendicular current dissipation through magnetic reconnection, and more gradual events (10-100 s) indicating parallel current dissipation via anomalous resistivity.

It is important to note that reconnection underlies both parallel and perpendicular processes, though operating under different plasma conditions. The spatial scales also differ substantially: reconnection requires extremely thin current sheets (~10-100 m), while parallel dissipation can occur in wider regions (~1 km) where the critical current density for anomalous resistivity is exceeded.

For low-corona parameters ($\beta \sim 1$), this gives $L_W \approx 300$ m for HRI_{EUV} eventsalready below the resolution limits achievable at Solar Orbiter's closest perihelia (100 km). However, the observed current sheets might be larger due to unresolved structure.

5.3. Evolution of Flare Detection Sensitivity and the Path to Fundamental Scales

The progression of occurrence rates across decades of solar observations reveals a remarkable trend in our ability to detect small-scale energy release events (Table 1). Our Solar Orbiter observations represent the latest milestone in this evolution:

- **1980s-1990s**: Hard X-ray instruments (Lin et al. 1984) and early EUV telescopes detected events at rates of $\sim 10^{-25}$–10^{-22} s^{-1} cm^{-2}
- **2000s**: TRACE and SOHO/EIT improved sensitivity to $\sim 10^{-22}$–10^{-21} s^{-1} cm^{-2}
- **2010s**: SDO/AIA and TESIS reached $\sim 10^{-21}$ s^{-1} cm^{-2}
- **2020s**: Solar Orbiter/EUI now achieves $\sim 10^{-20}$ s^{-1} cm^{-2}

This **five-order-of-magnitude increase** in detection capability over four decades demonstrates how each generation of instrumentation has revealed an increasingly dense population of small-scale energy releases. The fact that our $\geq 3\sigma$ detection rate (2.7×10^{-20} s^{-1} cm^{-2}) is approximately **60 times higher** than most previous quiet Sun studies and $\sim$ **100,000** times higher than early hard X-ray observations underscores the transformative capability of near-Sun observations with high spatial resolution and cadence.

This progression strongly supports Parker (1988a)'s prediction that improved instrumentation would reveal increasingly numerous small-scale energy releases, and suggests that future observations from even closer perihelia may reveal the fundamental heating events operating at the $\sim 10^{18}$ erg scale needed to completely explain coronal heating.

5.4. Current Sheet Formation and Dissipation Mechanisms

The formation and subsequent dissipation of current sheets represent fundamental processes in coronal energy release. Understanding both aspects is crucial for modeling picoflare energetics.

5.4.1. Current Sheet Formation Mechanisms

Multiple current sheet formation mechanisms can produce the picoflares observed in loop structures. Browning & Van der Linden (2003) provided strong support for Parker's framework by demonstrating that slow footpoint twisting drives coronal loops to a kink-instability threshold, triggering nanoflare-like reconnection. This mechanism aligns with our observations of picoflares in loop structures, particularly the intermittent brightenings along loop segments and single-loop events that suggest localized current dissipation from magnetic stress accumulation.

Current sheets can form via evolving X-points in both quiet (Syrovatskii 1971; Somov & Syrovatsky 1977; Demoulin et al. 1994) and active regions (Demoulin et al. 1994). Numerical MHD simulations demonstrate thin current layer formation under continuous photospheric driving (Longcope & Sudan 1992; Galsgaard 1996; Aulanier et al. 2005), with current sheet thicknesses scaling with the applied driving velocity and magnetic field geometry.

Turbulence cascades from photospheric driving also naturally produce current sheets at progressively smaller scales (Heyvaerts & Priest 1984; Dmitruk & Gómez 1997), underpinning modern coronal heating models (Gomez et al. 2000; Klimchuk 2017).

5.4.2. Current Sheet Dissipation Timescales and Mechanisms

Both parallel (field-aligned) and perpendicular (cross-field) currents ultimately dissipate via magnetic reconnection, but operate under different plasma conditions with distinct characteristic timescales.

Parallel Currents (Field-Aligned):

Parallel currents dissipate via anomalous resistivity when critical current density is exceeded. This collisionless process involves energy exchange through plasma waves (drift, ion-acoustic, or lower-hybrid waves) (Marsch 2006; Rosenbluth & Sagdeev 1983; Rosenbluth 1983; Galeev et al. 1984). Current-carrying electrons excite collective oscillations, transferring momentum to waves and reducing electron drift speeddissipating current analogously to Joule heating.

Dissipation commences when:

$$|\nabla \times \mathbf{B}| \approx \frac{B}{L_W} > \frac{4\pi}{c} n_e e c_S$$

where L_W is current sheet half-thickness, $c_S = \sqrt{T_e/m_i}$ is ion-sound speed. This yields:

$$L_W < \beta^{-1/2} \frac{c}{\omega_{pi}}$$

For low-corona parameters ($\beta \sim 1$), this gives $L_W \approx 300$ m for $\mathrm{HRI_{EUV}}$ eventsalready below the resolution limits achievable at Solar Orbiter's closest perihelia (100 km).

The characteristic timescale for parallel current dissipation is governed by wave-particle interactions:

$$\tau_{\parallel} \sim \frac{L}{c_S} \approx 10 - 100 \text{ s}$$

where $c_S = \sqrt{k_B T_e/m_i} \approx 50 - 150$ km/s is the ion sound speed for coronal temperatures. This slower dissipation produces more gradual heating events.

Perpendicular Currents (Cross-Field):

Perpendicular currents dissipate through magnetic reconnectionrapid reconfiguration converting magnetic energy to kinetic and thermal energy (Priest & Forbes 2000). It is important to note that reconnection underlies both parallel and perpendicular processes, though operating under different plasma conditions. The characteristic timescale is Alfvénic:

$$\tau_{\perp} \sim \frac{L}{V_A} \approx 1 - 10 \text{ s}$$

where $L \approx 10^3$–5×10^3 km is the current sheet length and $V_A \approx 1000$ km/s is the Alfvén speed. This rapid timescale produces the impulsive brightenings characteristic of reconnection events.

Key differences between the dissipation mechanisms include:

- *Topology change* vs. continuous deformation
- *Particle acceleration* vs. direct heating
- *Alfvénic timescales* vs. slower diffusive processes
- *Macroscopic outflows* and particle beams
- *Mass-dependent energy partition* in outflows

The spatial scales also differ substantially: reconnection requires extremely thin current sheets (∼10-100 m), while parallel dissipation can occur in wider regions (∼1 km) where the critical current density for anomalous resistivity is exceeded.

5.4.3. Observational Implications of Combined Formation and Dissipation

The different timescales have crucial observational implications: we expect to detect two distinct populations of picoflares. Rapid, impulsive events ($\tau \sim 1 - 10$ s) correspond to perpendicular current dissipation through magnetic reconnection, while more gradual, longer-duration events ($\tau \sim 10 - 100$ s) indicate parallel current dissipation via anomalous resistivity.

The diverse duration distribution observed in our picoflare sample (1-260 s) reflects this mixture of dissipation mechanisms operating in different plasma β regimes. This distinction helps explain the observed duration distribution and provides valuable guidance for future observational campaigns targeting these different dissipation mechanisms.

The observed picoflare characteristicsparticularly their compact sizes, low altitudes, and thermal energy dominancesuggest that both parallel and perpendicular current dissipation contribute significantly to coronal heating. Future modeling efforts should incorporate both formation and dissipation mechanisms to fully account for the energy budget and spatial distribution of coronal heating events.

The combination of high-resolution observations from Solar Orbiter and independent plasma parameter determination through stereoscopy provides an unprecedented opportunity to constrain these models. As we approach the fundamental scales of coronal heating, the distinction between different current sheet formation and dissipation mechanisms becomes increasingly important for understanding the energy balance of the solar atmosphere.

6. Conclusions

This work presents a comprehensive continuation of the analysis of the campfire events discovered by Berghmans et al. (2021), extending their statistical analysis to provide complete energy distributions and occurrence rates. Our analysis confirms the original event detection rates while providing the statistical characterization of the energy distribution, revealing occurrence rates that continue the historical trend of increasing small-scale event detection with improving instrumental capabilities.

Solar Orbiter is the first mission with high-resolution X-ray and EUV telescopes imaging the corona from within 1 AU, enabling the observation of previously unresolved small-scale and rapid variability. The detected picoflare rate of 2.7×10^{-20} s^{-1} cm^{-2} represents the highest occurrence rate yet measured for small-scale energy releases, continuing the progression from early hard X-ray observations ($\sim 10^{-25}$ s^{-1} cm^{-2}) through TRACE/SOHO era ($\sim 10^{-22}$–10^{-21} s^{-1} cm^{-2}) to the current near-Sun observations. On 30 May 2020, the HRI$_{\rm EUV}$ telescope, located halfway to the Sun, captured an ultra-quiet solar region at a cadence of a few seconds, revealing previously unresolved, morphologically diverse impulsive heating events (Berghmans et al. 2021). Our continuation of this dataset analysis demonstrates:

1. HRI$_{\rm EUV}$ sudden heating events observed in the 174 Å passband emit thermal energies of 3.4×10^{20}–9.8×10^{23} erg, identifying them as picoflares below previously established flare energy thresholds.
2. The picoflare frequency distribution for $\geq 3\sigma$ events is well-approximated by a power law $N(E_{\rm th}) \propto E_{\rm th}^{-2.74\pm0.23}$ with occurrence rate 2.7×10^{-20} s^{-1} cm^{-2}, which would need to extend down to $\sim 1.25\times10^{18}$ erg per event to satisfy quiet-Sun coronal heating requirements.
3. Picoflare geometric parameters are smaller than those of EUV nanoflares observed from 1 AU: linear dimensions by about an order of magnitude, and volumes by about three orders of magnitude.
4. The EMT relationship for picoflares follows $EM \propto T^{1.90\pm0.35}$ (for $T \approx 13$ MK), consistent with larger X-ray flares but at lower coronal temperatures.
5. The observed distribution of picoflare durations (1-260 s) suggests the presence of both rapid reconnection events (Alfvénic timescales, ∼1-10 s) and slower parallel current dissipation events (sound-speed timescales, ∼10-100 s), indicating multiple current dissipation mechanisms contribute to coronal heating at these small scales.
6. The observed picoflares contribute ∼1% of the total power needed to sustain the quiescent corona (including chromospheric and coronal losses), representing a previously unaccounted-for energy input.

Our analysis bridges the gap between the initial discovery of campfires by Berghmans et al. (2021) and theoretical predictions of coronal heating mechanisms, demonstrating that the solar corona hosts a continuum of energy release events spanning at least 15 orders of magnitude in energy. The high-frequency, low-energy picoflares detected by Solar Orbiter represent a significant component of the coronal energy budget, with their cumulative effect contributing substantially to quiet-Sun heating. Future observations from closer perihelia promise to reveal even smaller energy releases, potentially down to the 10^{16} erg scale predicted by theory.

Einaudi & Velli (1999) predicted 10^{16} erg heating events might be observable in the quiet corona at Solar Orbiter's closest approach (0.3 AU). Our continuation confirms that the energy distribution of flare energies extends to previously unobservable regimes, well-approximated by power-law behavior and supporting the nanoflare heating paradigm while opening new avenues for understanding the fundamental processes that maintain the million-degree solar corona.

Acknowledgements. The authors are grateful to the referee for their insightful comments, which improved the statistical significance analysis near detection thresholds and advanced the plasma physics understanding of current dissipation mechanisms, particularly regarding characteristic timescales of quasi-parallel current sheets. The authors wish to dedicate this paper to the memory of E. Parker for the discussions on quiet Sun coronal heating mechanisms, and to the memories of J.-P. Delaboudini'ere and S. Koutchmy. We are also indebted to EUI Principal Investigator D. Berghmans for his strong inspiration of this work. We further thank co-authors C. Verbeeck and M. Georgoulis for their generous support in preparing the revised version of the paper. The Solar Orbiter mission is a space mission of international collaboration between ESA and NASA, operated by ESA. The EUI instrument was built by a consortium led by CSL, and including IAS, MPS, MSSL/UCL, PMOD/WRC, ROB, and LCF/IO, with funding from the Belgian Federal Science Policy Office (BELSPO/PRODEX PEA 4000134088); the Centre National d'Etudes Spatiales (CNES); the UK Space Agency (UKSA); the Bundesministerium f"ur Wirtschaft und Energie (BMWi) through the Deutsches Zentrum f"ur Luft- und Raumfahrt (DLR); and the Swiss Space Office (SSO). The authors acknowledge the following specific support: The ROB team thanks BELSPO for support through the ESA-PRODEX program (grants 4000134088, 4000112292, 4000136424, and 4000134474). D.M.L. is grateful to the UK Science and Technology Facilities Council (STFC) for an Ernest Rutherford Fellowship (ST/R003246/1). P.A. acknowledges funding from an STFC Ernest Rutherford Fellowship (ST/R004285/2). O.P. is grateful to the German Leibniz Association and the MWFK Brandenburg. The work of F.S. was supported by DLR grant 50 OT 1904. A.M.V. and S.P. acknowledge the Austrian Science Fund (FWF): project I4555-N.

References

Aschwanden, M. J., Newmark, J. S., Delaboudinière, J.-P., et al. 1999, ApJ, 515, 842, doi: 10.1086/307036
Aschwanden, M. J., Nightingale, R. W., Tarbell, T. D., & Wolfson, C. J. 2000, The Astrophysical Journal, 535, 1027, doi: 10.1086/308866
Aschwanden, M. J., & Parnell, C. E. 2002, The Astrophysical Journal, 572, 1048, doi: 10.1086/340385
Aschwanden, M. J., Crosby, N. B., Dimitropoulou, M., et al. 2016, Space Science Reviews, 198, 47
Aulanier, G., Pariat, E., & Démoulin, P. 2005, A&A, 444, 961, doi: 10.1051/0004-6361:20053600
Battaglia, A. F., Saqri, J., Massa, P., et al. 2021, arXiv preprint arXiv:2106.10058
Benz, A., & Krucker, S. 1998, Sol. Phys., 182, 349
Benz, A. O., & Krucker, S. 2002, ApJ, 568, 413, doi: 10.1086/338807
Berghmans, D., Clette, F., & Moses, D. 1998, A&A, 336, 1039
Berghmans, D., Auchère, F., Long, D., et al. 2021, Astronomy & Astrophysics, 656, L4
Browning, P. K., & Van der Linden, R. A. M. 2003, Astronomy & Astrophysics, 400, 355, doi: 10.1051/0004-6361:20021887
Cargill, P. J., & Klimchuk, J. A. 2004, The Astrophysical Journal, 605, 911, doi: 10.1086/382526
Chitta, L. P., Peter, H., & Young, P. R. 2021, A&A, 647, A159, doi: 10.1051/0004-6361/202039969
Chitta, L. P., Zhukov, A. N., Berghmans, D., et al. 2023, Science, 381, 867, doi: 10.1126/science.ade5801
Chitta, L. P., Huang, Z., D'Amicis, R., et al. 2025, A&A, 694, A71, doi: 10.1051/0004-6361/202450233
Crosby, N. B., Aschwanden, M. J., & Dennis, B. R. 1993, Sol. Phys., 143, 275, doi: 10.1007/BF00646488
Demoulin, P., Henoux, J. C., & Mandrini, C. H. 1994, A&A, 285, 1023
Demoulin, P., & Klein, K.-L. 2000, in Transport and Energy Conversion in the Heliosphere, ed. J. P. Rozelot, L. Klein, & J. C. Vial, Vol. 553, 99
Démoulin, P., Priest, E., & Lonie, D. 1996, Journal of Geophysical Research: Space Physics, 101, 7631
Dmitruk, P., & Gómez, D. O. 1997, ApJ, 484, L83, doi: 10.1086/310760
Einaudi, G., & Velli, M. 1994, Space Sci. Rev., 68, 97, doi: 10.1007/BF00749122
—. 1999, Physics of Plasmas, 6, 4146, doi: 10.1063/1.873679
Fletcher, L., Dennis, B. R., Hudson, H. S., et al. 2011, Space science reviews, 159, 19
Galeev, A. A., Rosenbluth, M. N., & Sudan, R. N., eds. 1984, Basic Plasma Physics II (Amsterdam: North-Holland Physics Publishing)
Galsgaard, K. 1996, A&A, 315, 312
Gary, G. A. 2001, Solar Physics, 203, 71
Gold, T. 1964, in AAS/NASA, in the Physics of Solar Flares, NASA-SP 50, Hess W.N. (ed.), NASA, 39

Golub, L., Maxson, C., Rosner, R., Vaiana, G. S., & Serio, S. 1980, ApJ, 238, 343, doi: 10.1086/157990
Golub, L., & Pasachoff, J. M. 2010, The Solar Corona (Cambridge)
Gomez, D. O., Dmitruk, P. A., & Milano, L. J. 2000, Sol. Phys., 195, 299, doi: 10.1023/A:1005283923956
Hannah, I. G., Christe, S., Krucker, S., et al. 2008, The Astrophysical Journal, 677, 704, doi: 10.1086/529012
Hannah, I. G., & Kontar, E. P. 2012, A&A, 539, A146, doi: 10.1051/0004-6361/201117576
Harra, L. K., Gallagher, P. T., & Phillips, K. J. H. 2000, A&A, 362, 371
Heyvaerts, J., & Priest, E. R. 1984, A&A, 137, 63
James, T., & Subramanian, P. 2018, MNRAS, 479, 1603, doi: 10.1093/mnras/sty1610
James, T., Subramanian, P., & Kontar, E. P. 2017, MNRAS, 471, 89, doi: 10.1093/mnras/stx1461
Joulin, V., Buchlin, E., Solomon, J., & Guennou, C. 2016, A&A, 591, A148, doi: 10.1051/0004-6361/201526254
Klimchuk, J. A. 2006, Solar Physics, 234, 41
—. 2015, Philosophical Transactions of the Royal Society A: Mathematical, Physical and Engineering Sciences, 373, 20140256
Klimchuk, J. A. 2017, arXiv e-prints, arXiv:1709.07320. https://arxiv.org/abs/1709.07320
Koutchmy, S., Hara, H., Suematsu, Y., & Reardon, K. 1997, A&A, 320, L33
Krucker, S., & Benz, A. 1998, ApJ, 501, L213
Krucker, S., & Benz, A. O. 2000, Sol. Phys., 191, 341, doi: 10.1023/A:1005255608792
Lin, R. P., Schwartz, R. A., Kane, S. R., Pelling, R. M., & Hurley, K. C. 1984, ApJ, 283, 421
Litvinenko, Y. E. 1999, ApJ, 515, 435, doi: 10.1086/307001
Longcope, D. W., & Sudan, R. N. 1992, ApJ, 384, 305, doi: 10.1086/170874
Marsch, E. 2006, Living Reviews in Solar Physics, 3, 1
Müller, D., Zouganelis, I., St. Cyr, O. C., & Gilbert, H. R. 2019, A&A, this volume
Parenti, S., del Zanna, G., Petralia, A., et al. 2017, The Astrophysical Journal, 846, 25, doi: 10.3847/1538-4357/aa835f
Parker, E. N. 1972, ApJ, 174, 499
—. 1988a, ApJ, 330, 474, doi: 10.1086/166485
—. 1988b, ApJ, 330, 474, doi: 10.1086/166485
Parnell, C. E., & Jupp, P. E. 2000, The Astrophysical Journal, 529, 554, doi: 10.1086/308271
Parnell, C. E., & Jupp, P. E. 2000, ApJ, 529, 554
Petschek, H. 1964, in AAS/NASA, Symp. Physics of Solar Flares, Hess W.N. (ed.), NASA, Washington, DC, 425
Priest, E., & Forbes, T. 2000, Magnetic reconnection: MHD theory and applications (Cambride, Un. P.)
Priest, E. R. 1981, Solar flare magnetohydrodynamics (Springer)
Priest, E. R., Foley, C. R., Heyvaerts, J., et al. 1998, Nature, 393, 545
Purkhart, S., & Veronig, A. M. 2022, A&A, 661, A149, doi: 10.1051/0004-6361/202243234
Rochus, P., & et al. 2019, A&A, This Volume
Rosenbluth, M. N., ed. 1983, Handbook of Plasma Physics: Basic Plasma Physics, Volumes 1–2 (Amsterdam: NorthHolland)
Rosenbluth, M. N., & Sagdeev, R. Z., eds. 1983, Handbook of Plasma Physics: Physics of Laser Plasma, Volume 3 (Amsterdam: NorthHolland)
Rosner, R., Tucker, W. H., & Vaiana, G. S. 1978, ApJ, 220, 643, doi: 10.1086/155949
Serio, S., Peres, G., Vaiana, G. S., Golub, L., & Rosner, R. 1981, ApJ, 243, 288, doi: 10.1086/158597
Shimizu, T., & Tsuneta, S. 1997, ApJ, 486, 1045, doi: 10.1086/304542
Shimizu, T., Tsuneta, S., Acton, L. W., et al. 1994, ApJ, 422, 906
Somov, B., & Syrovatsky, S. 1977, Sol. Phys., 55, 393
Subramanian, S., Kashyap, V. L., Tripathi, D., Madjarska, M. S., & Doyle, J. G. 2018, A&A, 615, A47, doi: 10.1051/0004-6361/201629304
Syrovatskii, S. I. 1971, Sov. Phys. JETP, 33, 93
Ulyanov, A. S., Bogachev, S. A., Reva, A. A., Kirichenko, A. S., & Loboda, I. P. 2019, Astronomy Letters, 45, 248, doi: 10.1134/S1063773719040078
Verbeeck, C., Kraaikamp, E., Ryan, D. F., & Podladchikova, O. 2019, The Astrophysical Journal, 884, 50
Warmuth, A., & Mann, G. 2020, Astronomy & Astrophysics, 644, A172
Withbroe, G. L., & Noyes, R. W. 1977, ARA&A, 15, 363, doi: 10.1146/annurev.aa.15.090177.002051
Zhukov, A., Mierla, M., Auchère, F., et al. 2021, Astronomy & Astrophysics, 656, A35

[1] Igor Sikorsky Kyiv Polytechnic Institute, Peremohy Avenue, 37, 03056 Kyiv, Ukraine
[2] Leibniz Institute for Astrophysics Potsdam, An der Sternwarte 16, 14482 Potsdam, Germany
[3] Physikalisch-Meteorologisches Observatorium Davos, World Radiation Center, 7260 Davos Dorf, Switzerland
[4] ETH-Zürich, Wolfgang-Pauli-Str. 27, 8093 Zürich, Switzerland
[5] Solar-Terrestrial Centre of Excellence – SIDC, Royal Observatory of Belgium, Ringlaan -3- Av. Circulaire, 1180 Brussels, Belgium
[6] Institute of Geodynamics, Romanian Academy, 020032 Bucharest, Romania
[7] Université Paris-Saclay, CNRS, Institut d'Astrophysique Spatiale, 91405 Orsay, France
[8] Johns Hopkins University Applied Physics Laboratory, 11100 Johns Hopkins Rd, Laurel, MD 20723, USA
[9] Research Center for Astronomy and Applied Mathematics (RCAAM), Academy of Athens, 11527 Athens, Greece (on leave)
[10] Columbia Astrophysics Laboratory, Columbia University, 550 West 120th Street, New York, NY 10027, USA
[11] European Space Agency (ESA/ESTEC), 2200 AG Noordwijk, The Netherlands
[12] University of Graz, Institute of Physics, Universitätsplatz 5, 8010 Graz, Austria
[13] University of Graz, Kanzelhöhe Observatory for Solar and Environmental Research, 9521 Treffen, Austria
[14] Department of Mathematics, Physics and Electrical Engineering, Northumbria University, Newcastle Upon Tyne NE1 8ST, UK
[15] UCL-Mullard Space Science Laboratory, Holmbury St. Mary, Dorking, Surrey RH5 6NT, UK
[16] Skobeltsyn Institute of Nuclear Physics, Moscow State University, 119991 Moscow, Russia
[17] Department of Physics, Faculty of Science, University of Zanjan, 45195-313 Zanjan, Iran
[18] University of Applied Sciences and Arts Northwestern Switzerland, 5210 Windisch, Switzerland
[19] Institute of Applied Computing & Community Code, Universitat de les Illes Balears, 07122 Palma de Mallorca, Spain
[20] Davos Instruments AG, 7270 Davos Platz, Switzerland
[21] Max Planck Institute for Solar System Research, 37077 Göttingen, Germany
[22] European Space Agency (Spanish Space Law Centre), 28010 Madrid, Spain
[23] Centre Spatial de Liège, Université de Liège, 4031 Angleur, Belgium